Higher-Order Quantum Ghost Imaging with Ultracold Atoms

S. S. Hodgman,[*] W. Bu, S. B. Mann, R. I. Khakimov, and A. G. Truscott

Research School of Physics and Engineering, Australian National University, Canberra 2601, Australia

Ghost imaging is a quantum optics technique that uses correlations between two beams to reconstruct an image from photons that do not interact with the object being imaged. While pairwise (second-order) correlations are usually used to create the ghost image, higher-order correlations can be utilized to improve the performance. In this Letter, we demonstrate higher-order atomic ghost imaging, using entangled ultracold metastable helium atoms from an s-wave collision halo. We construct higher-order ghost images up to fifth order and show that using higher-order correlations can improve the visibility of the images without impacting the resolution. This is the first demonstration of higher-order ghost imaging with massive particles and the first higher-order ghost imaging protocol of any type using a quantum source.

Ghost imaging is an unconventional imaging method from quantum optics [1,2], which uses two correlated beams of photons. One beam interacts with the object, after which the arrival time (only) of each photon from the beam is detected on a "bucket" detector. The second photon from each pair, which never interacts with the object, is detected with full 3D spatial and temporal resolution on a multipixel detector. Using the correlations between the two beams, the image of the object can be reconstructed. While the technique was first theoretically proposed [3,4] and experimentally demonstrated [5,6] using light, it has since been extended to x rays [7,8], cold atoms [9], and electrons [10], along with a recent proposal involving neutrons [11]. The correlated nature of ghost imaging means that in certain circumstances, such as for weakly absorbing objects [12] or at low light levels [13,14], it can outperform conventional imaging. Ghost imaging has applications in a number of areas including optical encryption [15–17], improved telecommunications [18], and remote sensing [19,20], while the storage and retrieval of ghost images in atomic vapor cells [21] offers further potential applications. It also has the potential to reduce the dosage rates in imaging [22] and tomography [23] using radiation where potential damage to the sample from the radiation is a concern, such as x rays.

There are two distinct types of ghost imaging that have been demonstrated. Thermal or classical ghost imaging uses thermal or pseudothermal light, relying on semiclassical Hanbury Brown–Twiss (HBT) correlations to produce the images. In contrast, quantum ghost imaging uses a quantum source of correlated pairs, which for photons is usually spontaneous parametric down-conversion (SPDC). Although the SPDC pairs are entangled, entanglement is not necessary for ghost imaging [24,25], although the performance of the imaging by some measures may be improved with entanglement [26].

While the majority of ghost imaging implementations utilize pairwise (second-order) correlations, the basic schemes can be extended to employ higher-order correlations between more particles by incorporating additional detectors into the setup. This has been shown to improve the quality of key imaging parameters such as the visibility and contrast-to-noise ratio (CNR) [27,28], as well as the resolution [29], when implemented for ghost imaging with thermal light, due to the contribution of N-photon bunching [30]. However, due to the lower probability of higher-order correlated events being detected, in practical cases such improvements do not necessarily translate to performance gains over second-order ghost imaging when additional imaging improvements such as background subtraction are taken into account [31]. The use of higher-order correlations to enhance the performance of ghost imaging is similar to the increase in visibility of multiphoton interference from thermal light via higher-order correlations [32]. However, despite extensive work on higher-order thermal ghost imaging, to the best of our knowledge there has been no demonstration of higher-order ghost imaging for quantum light. This is partly because the relatively small two-photon bunching amplitude for thermal ghost imaging limits the achievable visibility to one-third, meaning that significant improvements are attainable using higher-order ghost imaging.

Here we demonstrate higher-order ghost imaging using correlated pairs of ultracold metastable helium (He*) atoms [33] from an s-wave scattering halo of two colliding Bose-Einstein condensates [34,35]. As shown in our previous work [9], by imposing a mask on one of the atoms in each pair we construct ghost images using the time correlations between those atoms and their corresponding correlated partners that are detected with full 3D resolution. In addition to the two-atom correlations due to pairwise scattering, there is a complex hierarchy of higher-order

correlations in the halo [36], and we use these to construct higher-order ghost images up to fifth order. The quality of the resulting images was characterized via the visibility and resolution, with higher-order imaging able to improve the visibility at no detriment to resolution.

The experimental procedure is similar to our previous method for second-order ghost imaging [9], with the starting point being a Bose-Einstein condensate (BEC) of $\approx 10^6$ helium atoms in the $m_J = +1$ sublevel of the long-lived 2^3S_1 metastable state [37], confined in a magnetic trap. A Raman pulse transfers nearly all atoms into the untrapped $m_J = 0$ state, while also imparting a momentum of $\mathbf{K} = -\sqrt{2}k_0\hat{\mathbf{z}}$ in the downwards direction (with gravity), where $k_0 = 2\pi/\lambda$ and $\lambda = 1083.2$ nm is the wavelength of the Raman laser. The untrapped BEC is then split into 12 momentum components, also in the $\hat{\mathbf{z}}$ direction, by a second diffraction pulse operating in the Kapitza-Dirac regime [9]. Each pair of BECs in adjacent momentum components then collide, producing a spherical halo with a radius (in the momentum space frame of reference centered on the two BEC components) of $k_r \approx k_0/\sqrt{2}$ comprising pairs of back-to-back correlated [34,36] and entangled [38] atoms, analogous to the pairs of photons produced from a SPDC source in quantum optics. Each of the 11 scattering halos has a radial Gaussian width of $w \approx 0.03k_r$, with an average mode occupancy varying from $n = 0.002(2)$ to $n = 0.08(1)$ across the halos, depending on the relative fraction of BEC atoms in each momentum mode. The multiple halos technique is used to reduce our data acquisition time, with the ghost imaging implemented for each halo separately. Within each halo there are correlations due to both the scattering collision and HBT style multiparticle interference (see Ref. [36] for details). In general, the higher orders have a higher degree of correlation, as measured by the amplitude of the relevant Nth order correlation function $g_{BB}^{(N)}$ [36], which represents the probability of finding atoms on directly opposed sides of the halo compared to anywhere else (see Refs. [36,39] for full definitions).

The halos fall under gravity ≈ 850 mm onto a multi-channel plate and delay-line detector, while also expanding during the fall time. This detector allows the full 3D position of the atoms at the detector, corresponding to the atomic momenta in the collision halo, to be measured with an x, y resolution of ~ 120 μm and a z resolution of ~ 12 μm ($\equiv 3$ μs in arrival time) [40]. The detector is divided in half centered on the halo, with one-half assigned as the bucket port and the other the "multipixel" port (see Fig. 1). A software mask [41] is imposed on the bucket port, so that only atoms in a defined region (the open area of the mask) are recorded. All spatial information of these bucket port atoms is then discarded, with only their arrival times retained. In the basic scheme of second-order ghost imaging, for each of these bucket port atoms (which have momentum $\mathbf{k} = k_x\hat{\mathbf{x}} + k_y\hat{\mathbf{y}} + k_z\hat{\mathbf{z}}$), any atom in the
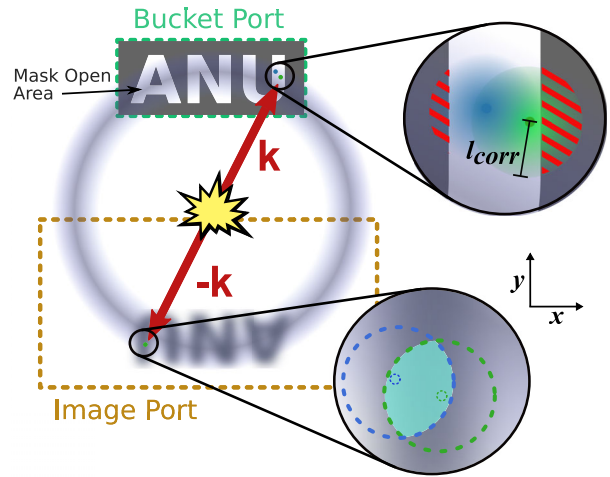

FIG. 1. Schematic of atomic higher-order ghost imaging. A halo (gray-shaded ring) of back-to-back correlated atoms is produced via pairwise s-wave collisions to produce correlated atoms with momenta $\mathbf{k}$ and $-\mathbf{k}$. The detector is divided in two, with atoms on the bucket port side of the halo passed through a mask (here ANU), with only the arrival times of atoms that pass through recorded and all spatial information of these atoms discarded. These arrival times are then correlated with the arrival times of atoms in the image port, which are measured with full 3D resolution, to match groups of 2, 3, 4, or 5 atoms around $\mathbf{k}$ and $-\mathbf{k}$, depending on the order of ghost imaging being used. The x and y components of these image port atoms form the ghost image. Insets show how higher-order imaging can improve the visibility: when an additional correlated atom (green dot in upper inset) beyond the first one (blue dot) is detected in the bucket port, the location of the second atom will most likely lie within a correlation length l_{corr} of the first one, although it must also pass through the mask, so the red shaded regions outside the mask open area are excluded. An atom detected in the image port, which is correlated with both bucket port atoms, is thus most likely to lie within the radius of the correlation length of the corresponding position of both of these (small dashed circles). This restricts image port atoms to a smaller area (indicated in cyan) than the area they could be found if there was only one correlated atom in the bucket port (either the large blue or green dashed circles). This makes the image atoms more likely to be located in the corresponding image region, rather than outside it, thus improving the visibility.

multipixel port that arrives within a time interval set by the correlation length of the scattered pairs ($l_{\text{corr}} \approx 0.03k_r$ [36], defined as the width of the volume in momentum space where the correlation function is peaked [39]) centered around $-k_z\hat{\mathbf{z}}$ is then added to the ghost image. The image is created from all correlated ghost image atoms across all 11 halos from $\sim 45\,000$ different experimental runs. Figure 2(a) shows a sample image of a mask of the letters "ANU."

For Nth-order ghost imaging the procedure is similar, with N total atoms for each detection event distributed in some particular combination around $k_z\hat{\mathbf{z}} + \mathbf{\Delta z}$ and $-k_z\hat{\mathbf{z}} + \mathbf{\Delta z}$, with all $|\mathbf{\Delta z}| < l_{\text{corr}}$. If this condition is met
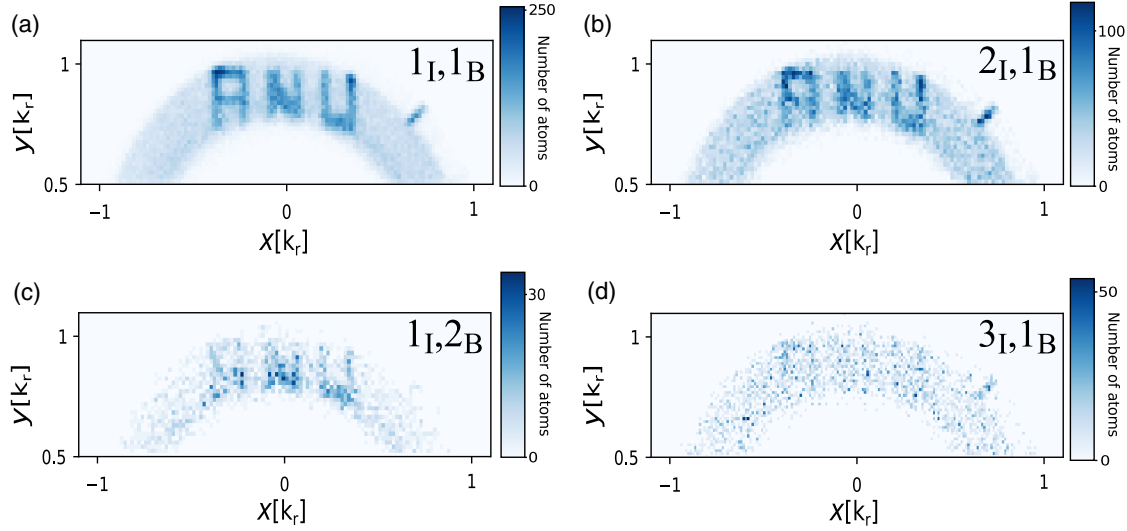
FIG. 2. A selection of atomic ghost images created using a transmission mask comprising the letters ANU. There is only one case (a) for second-order ghost imaging, consisting of 1 atom in each port (1_I, 1_B). In contrast, for three-atom ghost imaging there are two configurations, with either (b) two atoms in the image port (2_I, 1_B) or (c) two atoms in the bucket port (1_I, 1_B). Higher orders have correspondingly more possible configurations, of which one is shown (d) for four atoms, with three of these atoms detected in the image port (3_I, 1_B). The background semicircular arc corresponding to the halo is visible in each image and is due to random, uncorrelated atoms. The scale of the images is given in terms of the collisional recoil momentum k_r, while the number of atoms in each pixel is shown by the color bars for each image. All images are the result of ~45 000 experimental runs, and the increasingly stringent correlation criteria means that each image (a) to (d) has fewer total counts than the previous, leading to case (c) appearing less clear by eye than case (b), despite the calculated visibility being higher.

then all atoms around $-k_z\hat{\mathbf{z}}$ are added to the image. Each N has different possible combinations with varying degrees of correlation [36]. For example, in third-order ghost imaging one atom is always in each of the mask and the image, with the choice for the extra atom to be added to either port. Higher order extensions follow the same pattern. The two third-order cases are shown in Figs. 2(b) and 2(c), while the fourth-order case of three atoms in the image and one in the mask is shown in Fig. 2(d).

To quantitatively analyze and compare the performance of the different ghost imaging schemes, two widely used measures were calculated for each case: the visibility and the resolution. A rectangle mask of dimensions $(0.22 \times 0.18)k_r$ was used for both, to simplify the analysis.

The visibility V is defined as

$$V = \frac{I - B}{I + B}. \qquad (1)$$

I is the total number of atoms in the region of the ghost image corresponding to the open area of the mask on the opposite side of the halo, while B is the total number of atoms in the halo in the rest of the ghost image. The non-halo regions, where almost no atoms will be found, are excluded. Both I and B are normalized individually by the size of their respective areas.

The experimentally measured visibility for 8 different ghost imaging cases is shown in Fig. 3, representing all combinations up to fifth order (the two cases of fifth order

with 1 and 2 atoms in the image are not shown, as there were insufficient counts to produce a meaningful image). As the plot shows, the best visibility for each order N is achieved for one atom in the image port and the rest in the
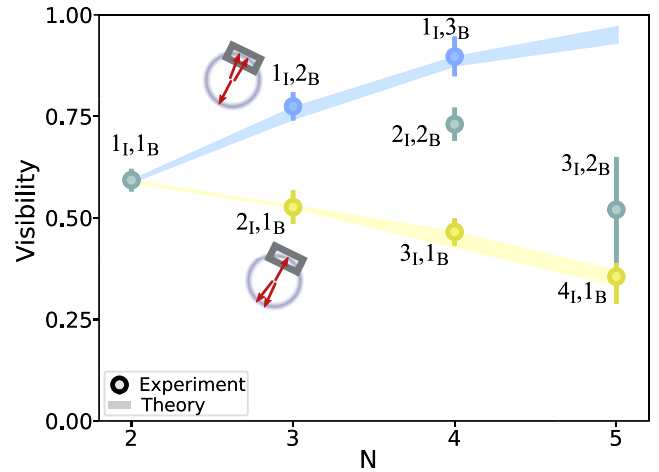

FIG. 3. The experimentally measured (circles) and numerically simulated (bands) visibilities for a range of different types and orders (N) of ghost imaging, with labels showing the number of atoms in the image (I) and bucket (B) ports, represented in the diagrams for the 3 atom cases. Blue visibilities are for the optimal cases, with one atom in the image port and the rest in the bucket (mask) port, with the reverse cases shown in yellow (green points are for intermediate cases). Error bars show the variance in intensity, due to shot-to-shot variations in B and I.
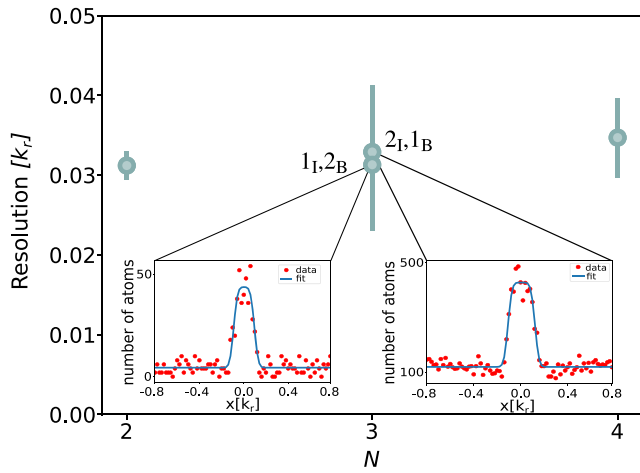
FIG. 4. Resolution of ghost imaging using different orders N. The resolution is calculated by forming a ghost image of a square mask, integrating along the y dimension and then fitting a Gaussian function convolved with a top hat of the width of the mask. Insets show these plots for the two third-order cases (the left inset shows the case of one atom in the image, the right inset is two atoms in the image). In all cases the resolution does not significantly change for different methods within error.

mask (blue points). For these cases V increases with N, while for the opposite case (one atom in the mask and the rest in the image) shown in yellow, V decreases with N. Intermediate cases (green) lie in between. The insets in Fig. 1 show schematically how higher-order ghost imaging can improve the visibility by increasing the overlap of the detection event locations and the mask.

In both extreme cases (blue and yellow in Fig. 3), the degree of correlation is the same. However, for higher-order schemes some intermediate (green) configurations are more correlated (e.g., for fourth order the $2_I, 2_B$ case has a higher degree of correlation than the other cases). This implies that the change in V is not primarily due to an increased degree of correlation, but the relative number of atoms in the image port and bucket port is more important. In the best case, more atoms in the mask increases the probability that the only atom in the image will be a correlated hit and not a background atom, as the atoms in the mask are limited to a smaller area. In contrast, there is a much larger area where atoms in the image port can possibly fall, and thus more background atoms are included. The trend of the extreme cases is similar to that observed with optics for multiphoton interference [32].

This interpretation of extra atoms in the image port increasing B, and this effect being more dominant than the relative bunching amplitude, is supported by numerical simulations [39]. The visibilities generated for our experimental parameters are shown as yellow and blue bands in Fig. 3, which agree well with the experimental results. Importantly, the simulations show that while an increased bunching amplitude $g_{BB}^{(N)}$ does improve visibility, for

$g_{BB}^{(N)} \sim 7$ this effect starts to saturate, whereas increasing $l_{\rm corr}$ always decreases the visibility. For the values of n in our experiments, $g_{BB}^{(N)} > 10$ and thus the optimal visibility is always with the maximum number of atoms in the bucket port.

The other image quality measure implemented was the resolution, which depends on the finite correlation length of the correlated atoms [9]. To measure the resolution the ghost image of a $(0.22 \times 0.18)k_r$ size rectangle for each case is integrated along the y axis. A 1D Gaussian convolved with a top-hat function of the size of the square mask was then fitted to the data and the width of the fitted Gaussian σ, which corresponds to the resolution of the image, extracted.

The measured resolutions for the different cases are shown in Fig. 4, along with some sample plots showing the raw data. For all cases the measured resolution is close to $l_{\rm corr}$. There is also little difference in the resolution for the different ghost imaging methods, although the resolution for higher-order cases with more atoms in the image may be slightly worse.

In conclusion, we have demonstrated higher-order ghost imaging with atoms up to fifth order, the first such demonstration with massive particles and the first higher-order ghost imaging experiment using a quantum source, to the best of our knowledge. The visibility was seen to improve with higher orders for the cases with only 1 atom in the image port while the reverse occurred for cases with only one atom in the mask, although in higher-order cases this can result in a small number of atoms in the resultant image. In all cases the resolution did not change significantly. Our demonstration paves the way to improve the visibility of thermal atomic ghost imaging using higher-order correlations. This could yield images with improved visibility at lower dosage rates to the sample being imaged for damage sensitive applications such as atomic ghost lithography, similar to the demonstrations with x-ray ghost imaging [7] and tomography [23]. By extending the higher-order atomic ghost imaging scheme presented here, complex fundamental tests of quantum mechanics with massive particles could also be possible, such as multiatom entanglement [42] or Bell's inequality measurement schemes [43] using 3 or more particles.

*sean.hodgman@anu.edu.au
[1] B. I. Erkmen and J. H. Shapiro, Ghost imaging: from quantum to classical to computational, Adv. Opt. Photonics **2**, 405 (2010).

[2] J. H. Shapiro and R. W. Boyd, The physics of ghost imaging, Quantum Inf. Process. **11,** 949 (2012).

[3] D. Klyshko, Effect of focusing on photon correlation in parametric light scattering,Zh. Eksp. Teor. Fiz. **94,** 82 (1988). [Sov. Phys. JETP **67,** 1131 (1988)].

[4] A. V. Belinskii and D. N. Klyshko, Two-photon optics: diraction, holography, and transformation of two-dimensional signals, Zh. Eksp. Teor. Fiz. **105,** 487 (1994). [Sov. Phys. JETP **78,** 259 (1994)].

[5] T. B. Pittman, Y. H. Shih, D. V. Strekalov, and A. V. Sergienko, Optical imaging by means of two-photon quantum entanglement, Phys. Rev. A **52,** R3429 (1995).

[6] D. V. Strekalov, A. V. Sergienko, D. N. Klyshko, and Y. H. Shih, Observation of Two-Photon "Ghost" interference and Diffraction, Phys. Rev. Lett. **74,** 3600 (1995).

[7] D. Pelliccia, A. Rack, M. Scheel, V. Cantelli, and D. M. Paganin, Experimental X-Ray Ghost Imaging, Phys. Rev. Lett. **117,** 113902 (2016).

[8] H. Yu, R. Lu, S. Han, H. Xie, G. Du, T. Xiao, and D. Zhu, Fourier-Transform Ghost Imaging with Hard X Rays, Phys. Rev. Lett. **117,** 113901 (2016).

[9] R. I. Khakimov, B. M. Henson, D. K. Shin, S. S. Hodgman, R. G. Dall, K. G. H. Baldwin, and A. G. Truscott, Ghost imaging with atoms, Nature (London) **540,** 100 (2016).

[10] S. Li, F. Cropp, K. Kabra, T. J. Lane, G. Wetzstein, P. Musumeci, and D. Ratner, Electron ghost imaging, Phys. Rev. Lett. **121,** 114801 (2018).

[11] K. Chen and S. Han, Microscopy for atomic and magnetic structures based on thermal neutron fourier-transform ghost imaging, arXiv:1801.10046.

[12] G. Brida, M. Genovese, and I. Ruo Berchera, Experimental realization of sub-shot-noise quantum imaging, Nat. Photonics **4,** 227 (2010).

[13] P. A. Morris, R. S. Aspden, J. E. C. Bell, R. W. Boyd, and M. J. Padgett, Imaging with a small number of photons, Nat. Commun. **6,** 5913 (2015).

[14] X. Shi, X. Huang, S. Nan, H. Li, Y. Bai, and X. Fu, Image quality enhancement in low-light-level ghost imaging using modified compressive sensing method, Laser Phys. Lett. **15,** 045204 (2018).

[15] L.-J. Kong, Y. Li, S.-X. Qian, S.-M. Li, C. Tu, and H.-T. Wang, Encryption of ghost imaging, Phys. Rev. A **88,** 013852 (2013).

[16] S. Yuan, J. Yao, X. Liu, X. Zhou, and Z. Li, Cryptanalysis and security enhancement of optical cryptography based on computational ghost imaging, Opt. Commun. **365,** 180 (2016).

[17] S. Li, X.-R. Yao, W.-K. Yu, L.-A. Wu, and G.-J. Zhai, High-speed secure key distribution over an optical network based on computational correlation imaging, Opt. Lett. **38,** 2144 (2013).

[18] P. Ryczkowski, M. Barbier, A. T. Friberg, J. M. Dudley, and G. Genty, Ghost imaging in the time domain, Nat. Photonics **10,** 167 (2016).

[19] B. I. Erkmen, Computational ghost imaging for remote sensing, J. Opt. Soc. Am. A **29,** 782 (2012).

[20] N. D. Hardy and J. H. Shapiro, Computational ghost imaging versus imaging laser radar for three-dimensional imaging, Phys. Rev. A **87,** 023820 (2013).

[21] Y.-W. Cho, J.-E. Oh, and Y.-H. Kim, Storage and retrieval of ghost images in hot atomic vapor, Opt. Express **20,** 5809 (2012).

[22] A.-X. Zhang, Y.-H. He, L.-A. Wu, L.-M. Chen, and B.-B. Wang, Tabletop x-ray ghost imaging with ultra-low radiation, Optica **5,** 374 (2018).

[23] A. M. Kingston, D. Pelliccia, A. Rack, M. P. Olbinado, Y. Cheng, G. R. Myers, and D. M. Paganin, Ghost tomography, Optica **5,** 1516 (2018).

[24] R. S. Bennink, S. J. Bentley, and R. W. Boyd, "Two-photon" coincidence imaging with a classical source, Phys. Rev. Lett. **89,** 113601 (2002).

[25] B. I. Erkmen and J. H. Shapiro, Unified theory of ghost imaging with gaussian-state light, Phys. Rev. A **77,** 043809 (2008).

[26] R. S. Bennink, S. J. Bentley, R. W. Boyd, and J. C. Howell, Quantum and Classical Coincidence Imaging, Phys. Rev. Lett. **92,** 033601 (2004).

[27] X.-H. Chen, I. N. Agafonov, K.-H. Luo, Q. Liu, R. Xian, M. V. Chekhova, and L.-A. Wu, High-visibility, high-order lensless ghost imaging with thermal light, Opt. Lett. **35,** 1166 (2010).

[28] H. Li, J. Shi, Z. Chen, and G. Zeng, Detailed quality analysis of ideal high-order thermal ghost imaging, J. Opt. Soc. Am. A **29,** 2256 (2012).

[29] Y. Zhou, J. Liu, J. Simon, and Y. Shih, Resolution enhancement of third-order thermal light ghost imaging in the photon counting regime, J. Opt. Soc. Am. B **29,** 377 (2012).

[30] Q. Liu, X.-H. Chen, K.-H. Luo, W. Wu, and L.-A. Wu, Role of multiphoton bunching in high-order ghost imaging with thermal light sources, Phys. Rev. A **79,** 053844 (2009).

[31] K. W. C. Chan, M. N. O'Sullivan, and R. W. Boyd, Optimization of thermal ghost imaging: high-order correlations vs. background subtraction, Opt. Express **18,** 5562 (2010).

[32] I. N. Agafonov, M. V. Chekhova, T. S. Iskhakov, and A. N. Penin, High-visibility multiphoton interference of hanbury brown–twiss type for classical light, Phys. Rev. A **77,** 053801 (2008).

[33] W. Vassen, C. Cohen-Tannoudji, M. Leduc, D. Boiron, C. I. Westbrook, A. Truscott, K. Baldwin, G. Birkl, P. Cancio, and M. Trippenbach, Cold and trapped metastable noble gases, Rev. Mod. Phys. **84,** 175 (2012).

[34] A. Perrin, H. Chang, V. Krachmalnicoff, M. Schellekens, D. Boiron, A. Aspect, and C. I. Westbrook, Observation of Atom Pairs in Spontaneous Four-Wave Mixing of Two Colliding Bose-Einstein Condensates, Phys. Rev. Lett. **99,** 150405 (2007).

[35] J.-C. Jaskula, M. Bonneau, G. B. Partridge, V. Krachmalnicoff, P. Deuar, K. V. Kheruntsyan, A. Aspect, D. Boiron, and C. I. Westbrook, Sub-poissonian number differences in four-wave mixing of matter waves, Phys. Rev. Lett. **105,** 190402 (2010).

[36] S. S. Hodgman, R. I. Khakimov, R. J. Lewis-Swan, A. G. Truscott, and K. V. Kheruntsyan, Solving the Quantum Many-Body Problem via Correlations Measured with a Momentum Microscope, Phys. Rev. Lett. **118,** 240402 (2017).

[37] S. S. Hodgman, R. G. Dall, L. J. Byron, K. G. H. Baldwin, S. J. Buckman, and A. G. Truscott, Metastable Helium: A New Determination of the Longest Atomic Excited-State Lifetime, Phys. Rev. Lett. **103,** 053002 (2009).

[38] D. K. Shin, B. M. Henson, S. S. Hodgman, T. Wasak, J. Chwedenczuk, and A. G. Truscott, A strong Bell correlation witness between spatially separated pairs of atoms, arXiv:1811.05681.

[39] See Supplemental Material at http://link.aps.org/supplemental/10.1103/PhysRevLett.122.233601 for details.

[40] B. M. Henson, X. Yue, S. S. Hodgman, D. K. Shin, L. A. Smirnov, E. A. Ostrovskaya, X. W. Guan, and A. G. Truscott, Bogoliubov-cherenkov radiation in an atom laser, Phys. Rev. A **97**, 063601 (2018).

[41] The mask is imposed in software to allow greater flexibility in analyzing with different masks, since to install a mask physically into the system requires bringing the ultrahigh vacuum detection chamber up to atmospheric pressure and then resealing and baking, meaning each mask installation requires nearly a week of experimental downtime. This software mask procedure has been shown to yield equivalent results to a physical mask when a mask was implemented with the same dimensions as in our previous ghost imaging experimental setup [9].

[42] J. Kofler, M. Singh, M. Ebner, M. Keller, M. Kotyrba, and A. Zeilinger, Einstein-podolsky-rosen correlations from colliding bose-einstein condensates, Phys. Rev. A **86**, 032115 (2012).

[43] B. Jack, J. Leach, J. Romero, S. Franke-Arnold, M. Ritsch-Marte, S. M. Barnett, and M. J. Padgett, Holographic Ghost Imaging and the Violation of a Bell Inequality, Phys. Rev. Lett. **103**, 083602 (2009).